Soot particle size distributions in turbulent opposed jet flames with premixed propene–air reactants

H. Shariatmadar, R.P. Lindstedt*

Department of Mechanical Engineering, Imperial College, London SW7 2AZ, UK

Abstract

Emissions of soot are strongly dependent on turbulence-chemistry interactions due to the relatively slow formation and oxidation processes. Studies of laminar flames have shown that both flow conditions and the chemistry of the parent fuel have a significant impact on measured particle size distributions (PSDs). The current study determines the impact of flow on the development of PSDs in premixed turbulent flames through a variation in the total rate of strain using an opposed jet configuration with fractal grid generated turbulence. The impact of fuel chemistry is investigated under such conditions through the use of propene–air flames with results compared to the corresponding ethene–air flames quantified in earlier studies. Samples were extracted using a quartz probe featuring aerodynamic quenching and dual port dilution at the probe tip and in the transfer-line. Spatially resolved PSD data is obtained along the stagnation point streamline using a scanning mobility particle sizer equipped with nano- and long-DMA columns to show the evolution through the turbulent flame brush. Results confirm that PSDs of soot in premixed turbulent flames are exceptionally sensitive to both the chemistry of the parent fuel and the flow field. The reduced residence times in the current turbulent flows lead to maximum median and mean mobility diameters below 10 nm with higher rates of strain promoting unimodal PSD shapes. It is further shown that the chemistry of the parent fuel has a strong influence on PSDs with propene causing a two order of magnitude increase in smaller particles compared to the corresponding ethene flame.

1. Introduction

Legal limits on combustion generated particulates are evolving from mass-based criteria towards more refined measures that require an understanding of soot formation processes to the point where soot particle size distributions (PSDs) can be measured and predicted in turbulent flames. Quantitative data on the evolution of soot PSDs for different fuel structures and flow conditions during turbulent combustion are accordingly necessary [1]. Recent experimental data of PAH formation in pre-

* Corresponding author.:.
E-mail address: p.lindstedt@imperial.ac.uk (R.P. Lindstedt).

mixed sooting turbulent ethene–air flames highlighted an extreme sensitivity to the flow field [2,3].

Experimental studies of PSDs in turbulent flames are exceptionally scarce. Boyette et al. [4] obtained soot PSDs for non-premixed ethene-jet flames at Reynolds numbers of 10,000 and 20,000 and show that the mean particle size remains below 10 nm and that the growth in the mean diameter along the centreline is proportional to the distance from the nozzle outlet. de Oliveira et al. [5] utilised a scanning mobility particle sizer (SMPS) to measure the size and number of nanoparticles at the outlet of a kerosene-fuelled spray combustor. The results indicate that the total soot volume fraction and the absolute number of particles increased with the core injection of air. Kazemimanesh et al. [6] determined the number density and median mobility diameter for heavy fuel mixtures in buoyant turbulent diffusion flames. Shariatmadar et al. [7] used SMPS to study the PSD evolution in premixed turbulent ethene–air flames crossing the soot inception limit using an opposed jet configuration. It was found that turbulent transport distributes soot particles across the mixing layer between the two jets with the maximum median and mean mobility diameters close to the stagnation point.

Examples of computational studies of soot PSDs include the work by Gkantonas et al. [8] who applied a sectional model coupled with a Conditional Moment Closure and Large Eddy Simulation to analyse the PSD evolution in a Rich-Quench-Lean (RQL) combustor burning ethene. The results show a broadly sustained unimodal PSD shape with a decreased particle size when air dilution is increased. Tian et al. [9] used a fully coupled sectional model featuring a 78-dimensional Joint-scalar PDF (JPDF) approach and a simplified nucleation model to investigate soot dynamics in a turbulent piloted non-premixed ethene flame to show that local extinction can lead to the transport of soot to cold fuel lean mixtures. Schiener and Lindstedt [10] showed that the experimental PSD data of Boyette et al. [4] could be predicted using this approach. Lucchesi et al. [11] performed simulations using a Direct Simulation Monte Carlo (DSMC) method to analyse the evolution of PSDs in turbulent sooting flames. It was shown that the turbulence leads to a broadening of PSDs with unimodal profiles compared to a strong bimodality in laminar flames.

The evolution of soot PSDs under laminar conditions provide insight into the underlying chemical processes. For example, Lin et al. [12] show that soot nucleates and grows quantitatively more quickly in propene flames compared to ethene flames under comparable conditions. Faster particle growth in flame with ethene/propene mixtures has been observed and attributed to synergistic effects [13]. Lin et al. [14] used SMPS coupled with a micro-orifice probe to study the PSD evolution

in a stagnation flow configuration and showed a PSD evolution from unimodal to bimodal distributions for gasoline and heptane/toluene flames. Shao et al. [15] investigated the impact of ammonia addition on PSDs in ethene laminar premixed flames. The results indicated that the addition of ammonia delayed nucleation with soot volume fractions reduced by ammonia doping. Studies using laminar flames clearly indicate that the parent fuel (or the fuel blends) has a principal influence on the PSDs evolution even in the absence of aromatic fuel components.

The brief summary above indicates strongly that both chemistry and flow control the evolution of PSDs of soot. As highlighted, quantitative experimental data on PSDs in turbulent flames is severely limited due to experimental difficulties. In the current work, the evolution of PSDs in premixed turbulent propene–air flames is determined using the opposed jet configuration of Shariatmadar et al. [2] with spatially resolved data obtained along the stagnation point streamline. Furthermore, the impact of the chemistry of the parent fuel on the evolution of PSDs is quantified by comparisons with the corresponding ethene–air flames [7].

2. Experimental setup

2.1. Burner configuration and experimental conditions

The current opposed jet configuration facilitates precise control of reactant mixtures and turbulent timescales [16] with premixed propene–air mixtures from the upper nozzle (UN) stabilised against hot combustion products (HCP) from the lower nozzle (LN) as illustrated in Fig. 1. The distance between the nozzles (30 mm) is set to one diameter [17] and a fractal grid is located 50 mm upstream of the UN exit to generate well developed multi-scale turbulence [18]. Opposed jet flows show anisotropy and a tendency to large-scale instabilities. The use of fractal grid generated turbulence removes the latter as shown by turbulence spectra [18] and the application of conditional proper orthogonal decomposition [19]. The anisotropy has also been carefully analysed [18,19] and the method used [20] to determine the rate of dissipation is based on the spatial derivatives of radial and axial velocities and should hence account (approximately) for the anisotropy. In the current flow, the turbulent rate of strain contribution dominates by factors from 2.2 to 3 as shown in Table 1. The HCP temperature (T_{HCP} = 1500 K) is generated from a nitrogen diluted stoichiometric hydrogen–air flames with a reactant mole fraction ratio $x_{H2}/x_{N2} = 0.51$. A perforated plate (PP) is installed 100 mm upstream of the LN exit [21] and used to stabilise multiple flames leading to a uniform HCP flow with the exit tem-
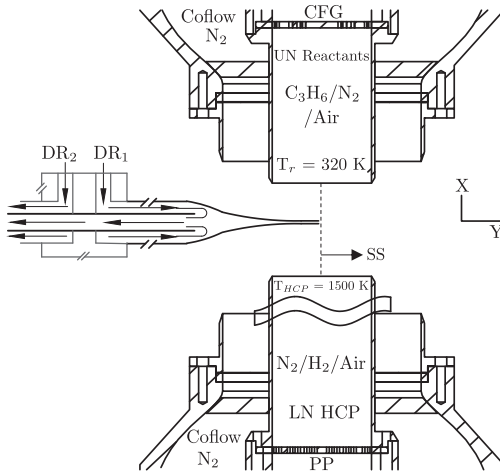
Fig. 1. A schematic of the current opposed jet burner and probe tip configuration used to measure particle size distribution. Premixed propene/air at a temperature $T_r = 320$ K is introduced from the upper nozzle (UN) with the resulting flame aerodynamically stabilised against hot combustion products (HCP) emerging from the lower nozzle (LN) at $T_{HCP} = 1500$ K. X – axial coordinate, Y – radial coordinate, CFG – cross fractal grid, PP – perforated plate, SS – stagnation streamline, DR_1 – probe tip dilution ratio, DR_2 – transfer line dilution ratio.

Table 1
Conditions used to study the impact of the rate of strain on PSDs in turbulent premixed propene–air flames at constant $\phi_{UN} = 2.0$ and $T_{HCP} = 1500$ K, where a_b [s^{-1}] is the bulk rate of strain, a_t [s^{-1}] the turbulent rate of strain, a_T [s^{-1}] the total rate of strain, Re$_t$ [-] the turbulent Reynolds number, U [m s^{-1}] the mean exit velocity of the upper nozzle reactants, u' [m s^{-1}] the corresponding turbulent fluctuations and τ_I [ms] the estimated integral time scale of turbulence.

Parametric variation						
a_b	90	110	120	140	160	180
a_t	200	265	300	375	450	540
a_T	290	375	420	515	610	720
Re$_t$	55	65	72	83	94	106
U	1.35	1.65	1.8	2.1	2.4	2.7
u'	0.23	0.27	0.3	0.34	0.39	0.44
τ_I	17.8	15.2	13.7	12.1	10.5	9.3

perature measured using a 50 μm R–type thermocouple [22]. Both nozzles are equipped with concentric nitrogen shrouds to shield the flames and the momentum of the HCP stream adjusted to locate the stagnation point at the nominal mid-point location.

The midpoint reference condition is selected as the flame with an equivalence ratio $\phi_{UN} = 2.0$ and a bulk rate of strain ($a_b = 2U/H$) of 120 s^{-1}. The total rate of strain ($a_T = a_b + a_t$) was estimated using the approach of Kostiuk et al. [23] with $a_t = (\varepsilon_r/\nu_r)^{1/2}$, where ε_r is the rate of dissipation in the reac-
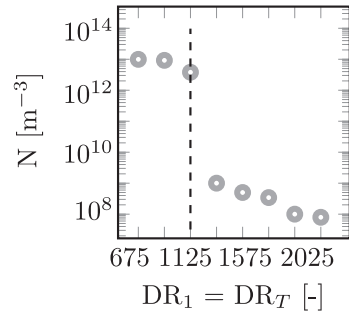

Fig. 2. The total number densities obtained using long–DMA ($8 \leq D_m$(nm) ≤ 230) with $DR_2 = 0$ for the reference flame ($\phi_{UN} = 2.0$, $T_{HCP} = 1500$ K, $a_T = 420$ s^{-1}). The total dilution ratio is $DR_T = DR_1$ for this case.

tants, determined using the method of George and Hussein [20] as applied by Goh et al. [19], and ν_r the corresponding fluid viscosity.

2.2. Estimate of reaction zone residence time

Laminar flame calculations were analysed to estimate the time scales available for soot particle growth and oxidation. The boundary conditions for the computational study matched the experimental data with reactant compositions and inlet temperatures obtained from corresponding ethene–air flames used as a comparison (see below). The computational domain was also identical to that of the experimental configuration with the exception that the flow is laminar. Hence, only the impact of bulk strain (not turbulent strain) can be accounted for accurately. However, the computations include the addition of the mean turbulent rate of strain by adjusting the reactant velocities to match the estimated total rate of strain (a_T) given in Table 1 to provide a better indication of the flame behaviour. The computational domain was resolved by 233 distributed cells with local refinement in the reaction zone providing a resolution of 36 μm. A detailed chemical mechanism featuring 358 species and 1789 reactions [24] was applied. The laminar flame data is only used to provide an estimate of the mean flow residence time for each experimental condition in order to support data interpretation. An example of a computed velocity profile is given in the Supplemental Material and all the residence times (t_r) have been computed starting at $X/L_I = 2.0$ which corresponds to the beginning of the turbulent flame brush [2].

2.3. Sampling probe and system

Probe configurations (e.g. shape and material), sampling methods and dilution ratios applied to withdraw soot samples differ significantly

Table 2
The optimal total dilution ratios for PSD measurements.

a_T [s^{-1}]	290	375	420	515	610	720
DR_T [-]	900	945	1125	1035	855	810

in the literature. Camacho et al. [25] used a tubular steel sampling probe (tip diameters from 0.13 to 0.16 mm) and optimised single-port dilution, while de Oliveira et al. [5] used a coxial stainless steel probe (tip diameter 0.50 mm) with single-port nitrogen dilution and a constant dilution ratio of 100 for different experimental conditions. Boyette et al. [4] used a tubular steel sampling probe (tip diameter 0.50 mm) and two-stage dilution to reduce losses in the extraction line. The burner configurations and experimental conditions differ significantly between studies. Camacho et al. [25] considered laminar opposed jet flames. Boyette et al. [4] studied coflow turbulent jet flames, while de Oliveira et al. [5] studied a combustor with azimuthally arranged fuel sprays at the upstream boundary and reverse flow air jets downstream.

The current sampling system is identical to that used by Shariatmadar et al. [2,3] and features a quartz probe (manufactured by Hilgenberg GmbH) and dual-port nitrogen dilution (see Fig. 1) at the probe tip and in the transfer-line combined with optimised mixture dependent dilution ratios to minimise losses. The aerodynamic probe has a tip orifice diameter of 286 µm and an opening angle of 20 degrees designed to minimise flame disturbances. Probe effects and potential clogging have been discussed by Shariatmadar et al. [2,3]. Two large vacuum chambers with a total volume of 36.8 litres are used to eliminate pressure fluctuations or a drift in the sampling pressure with a differential of 20 mbar between the sampling line and the flame set using a vacuum regulator, providing a constant sample flow rate of 3.125×10^{-6} kg/s. A pressure transducer (UNIK 5000; GE Measurement and Control) is used in the transfer line to monitor the static pressure. The probe tip is placed along the theoretical stagnation point streamline and aligned using an elastic light scattering (ELS) setup [2]. The sampling position is varied from the reactants towards the HCP stream. A sampling time of 120 s, corresponding to around 10,000 integral time scales of turbulence ($\tau_I = L_I /u$') was used to ensure statistical independence, with $\tau_I \simeq 13.7$ ms for the reference flame. Collection was terminated by disconnecting the probe from the vacuum system.

2.4. Sampling process

The nitrogen used for sample dilution is controlled via mass flow controllers with the dilution ratio determined by regulating the balance between the bypass pressure using a metering valve, a vac-
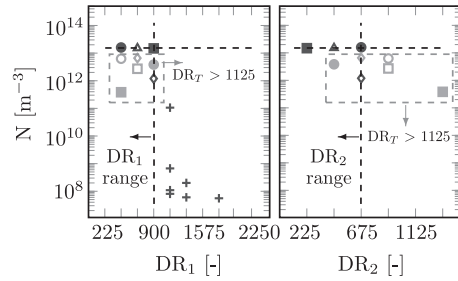

Fig. 3. Total number densities obtained using long-DMA ($8 \leq D_m$(nm) ≤ 230) versus dilution ratio at $\phi_{UN} = 2.0$, $a_T = 420$ s^{-1} and $T_{HCP} = 1500$ K. + symbol: Unacceptable sets; Black circle – $DR_1 = 450$ and $DR_2 = 675$; Black triangle – $DR_1 = 675$ and $DR_2 = 450$; Black square – $DR_1 = 900$ and $DR_2 = 225$; Open grey circle – $DR_1 = 450$ and $DR_2 = 900$; Grey square – $DR_1 = 450$ and $DR_2 = 1350$; Grey diamond – $DR_1 = 675$ and $DR_2 = 675$; Open grey square – $DR_1 = 675$ and $DR_2 = 900$; Grey circle – $DR_1 = 900$ and $DR_2 = 450$; Black diamond – $DR_1 = 900$ and $DR_2 = 675$..
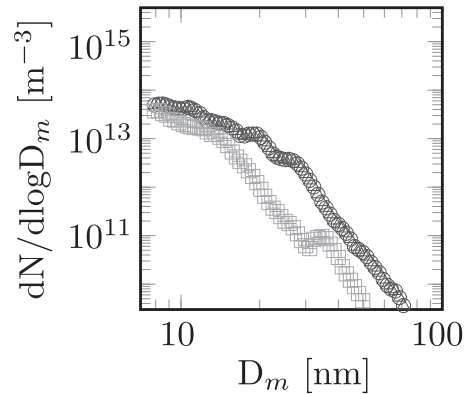

Fig. 4. The PSDs of two repeated samples obtained at various rates of strain at constant $\phi_{UN} = 2.0$ and $T_{HCP} = 1500$ K. Black circle and triangle – $a_T = 515$ s^{-1}. Grey square and plus symbol – $a_T = 720$ s^{-1}. The probe tip is located at $X/L_I = 0$.

uum regulator, and the SMPS vacuum pump pressure. The selected pressure differential of 20 mbar between the sampling line and the flame has been shown to minimise flow disturbances [2,3].

A extensive parametric study [7] of the impact of the dilution ratio on measured PSDs indicates that particle losses in the sampling line can be effectively eliminated using the current two-stage dilution process. The first dilution port is used to quench particles at the probe tip and the second dilution port increases the total sample dilution achievable and thus minimises particles losses in the transfer line.

The SMPS spectrometer system consists of an electrostatic classifier (TSI 3082), a neutralizer (TSI 3088), differential mobility analyzer (DMA), a
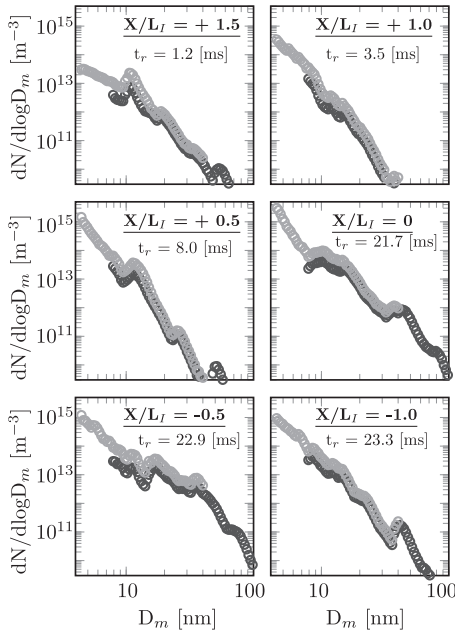
Fig. 5. The PSD profiles for nano-SMPS (grey) and long-DMA (black). The experiment is carried out at $\phi_{UN} = 2.0$, $a_T = 290$ s^{-1} and $T_{HCP} = 1500$ K. $X/L_I > 0$ is towards reactants and $X/L_I < 0$ towards the hot combustion products.

Fig. 6. The PSD profiles for nano-SMPS (grey) and long-DMA (black). The experiment is carried out at $\phi_{UN} = 2.0$, $a_T = 420$ s^{-1} and $T_{HCP} = 1500$ K. $X/L_I > 0$ is towards reactants and $X/L_I < 0$ towards the hot combustion products.

nano enhancer (TSI 3777) and a condensation particle counter (TSI 3772). Different setups were used depending on the particle size of interests with long– (model 3081) and nano– (model 3086) DMA used to enable the determination of a wide range of particle sizes. During mobility measurements, the sample and sheath flow through the nano–DMA and long–DMA were 1.5 and 15 L/min, respectively. An impactor with a nozzle size of 0.071 cm was used to provide flow rates that allow for particles to be classified in the ranges 4–40 nm and 8–230 nm for nano–DMA and long–DMA, respectively. Diethylene glycol (DEG $\geq$ 99%) and 1-butanol ($\geq$ 99.4%) were used as working fluids for the condensation particle counter (CPC) and nano-enhancer. A water removal system was used to remove contamination of the working fluids by condensed water vapour.

3. Optimal sampling conditions

For a given pressure differential (ΔP), the dilution ratio is calculated according to Eq. (1) using metered volumetric flow rates and a viscosity correction in the manner of Camacho et al. [25],

$$\text{DR} = \left(\frac{Q_s}{Q_{air}} \right) \left(\frac{T_0}{T_s} \right) \left(\frac{\mu_{m,f}}{\mu_{air}} \right) \tag{1}$$
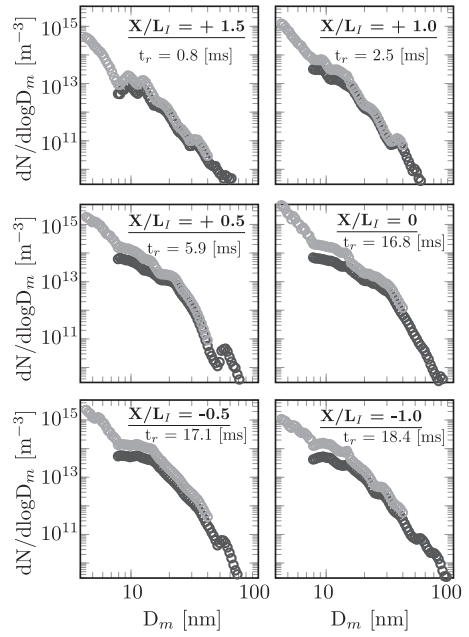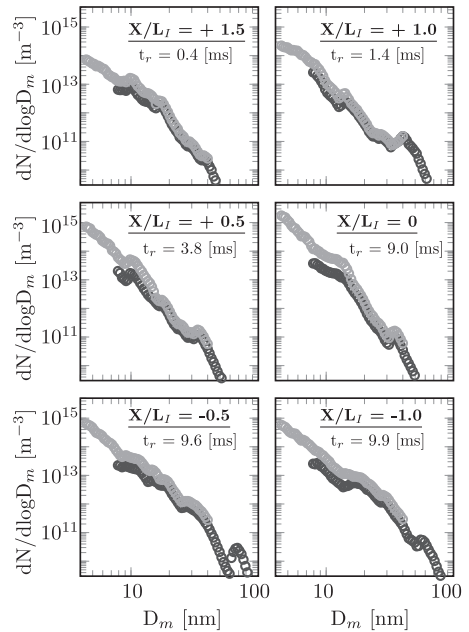

Fig. 7. The PSD profiles for nano-SMPS (grey) and long-DMA (black). The experiment is carried out at $\phi_{UN} = 2.0$, $a_T = 720$ s^{-1} and $T_{HCP} = 1500$ K. $X/L_I > 0$ is towards reactants and $X/L_I < 0$ towards the hot combustion products.

where Q_s and Q_{air} are the volumetric flow rates of the nitrogen diluent and the air drawn into the orifice, respectively. The temperature of the diluent gas is T_0 (= 300 K) and T_s ($\simeq$ 1508 K) that of the sample drawn into the probe orifice. The latter was determined using laminar flame computations [2] and based on the location $X/L_I = 0$. The dynamic viscosities $\mu_{m,f} = 3.12 \times 10^{-5}$ kg m^{-1} s^{-1} and $\mu_{air} = 1.84 \times 10^{-5}$ kg m^{-1} s^{-1} correspond to the flame and surrounding air. The impact of nitrogen dilution ratios on PSDs and the total number density obtained using long–DMA ($8 \leq D_m$(nm) ≤ 230) are presented separately for probe tip (DR_1), sampling line (DR_2) and total dilution (DR_T) ratios. Experiments are repeated at least five times for each condition to ensure reproducibility of results. The impact of sampling conditions on PSDs and the total number density is reported below for the reference flame condition.

3.1. The impact of probe tip dilution (DR_1)

The total number density for different amounts of probe tip dilution (DR_1) is depicted in Fig. 2 when $DR_2 = 0$ is used. The total number density reduces sharply for $DR_1 > 1125$ with N [m^{-3}] < 10^9. A limiting value of $DR_1 \leq 1125$ was selected for probe tip dilution. A more modest decrease in the total number density occurs for $900 \leq DR_1 \leq 1125$ and the impact of DR_2 on PSDs was accordingly investigated with $DR_1 \leq 900$.

3.2. The impact of transfer line dilution (DR_2)

The appropriate ranges for DR_1 and DR_2 are indicated in Fig. 3 using vertical dashed lines. The horizontal dashed lines represent the maximum total number density with lower values indicating particle losses. Only data sets obtained with $DR_1 \leq 900$ resulting in particle numbers N [m^{-3}] > 10^9 are shown. The results indicate particle losses for $DR_2 > 675$.

3.3. The impact of the total sample dilution (DR_T)

The overall sampling conditions are considered optimised when particles are not agglomerating or lost in the sampling process and when the total number density is insensitive to the applied dilution. The optimal values for probe tip and transfer line dilution are linked through the resulting total amount of dilution. As shown in Fig. 3, the total number density is constant with $DR_T = 1125$ for a number of data sets including (i) $DR_1 = 675$ and $DR_2 = 450$, (ii) $DR_1 = 900$ and $DR_2 = 225$, and (iii) $DR_1 = 450$ and $DR_2 = 675$. Subsequently, the optimum dilution ratios for all flames were identified using $DR_1 \leq 900$ and $DR_1 \leq 675$ and a constant transfer line dilution $DR_2 = 675$. The more sensitive probe tip dilution was adjusted depending on

the rate of strain to provide the total dilution ratios listed in Table 2.

3.4. Reproducibility of PSD measurements

Multiple charge and diffusion corrections are applied to rectify losses within the SMPS instruments [26]. The former is mainly evident for particles with $D_p > 100$ nm. The latter is mainly noticeable for particles with $D_p < 100$ nm. The reproducibility of the measurements was evaluated by repeating the sampling five times at constant flame and measurement positions. Fig. 4 shows the PSDs of two repeated samples obtained at $X/L_I = 0$ for $a_T = 515$ and 720 s^{-1}.

4. Spatially resolved particle size distributions

The SMPS scans were performed at multiple axial locations along the stagnation point streamline at intervals of 2 mm (~ 0.5 L_I). The absolute particle size distributions are provided in Figs. 5 – 7 for both nano– and long–DMA configurations and for the reference and limiting flames at total rates of strain $a_T = 290$, 420 and 720 s^{-1}. The PSDs for the intermediate experimental conditions are presented in the Supplemental Material. The maximum difference between the two DMA configurations is a factor of three. No differences in PSDs were observed for scan times above 30 seconds.

Figs. 6 and 7 show that the PSDs develop an essentially unimodal shape as the rate of strain is increased. The appearance of unimodal PSDs is accordance with the behaviour suggested by experimental and computational studies e.g. [4,8–11]. However, there is a notable flattening of the PSD and signs of bimodality at some measurement locations e.g. around $X/L_I \sim 0$. This trend is stronger at the lowest rate of strain as shown in Fig. 5, where a distinct bimodality is developing. Accordingly, it is likely that a flow condition dependent transition between unimodal and bimodal PSDs will take place in turbulent premixed flames with the latter increasingly favoured in low strain regions. The estimated residence times confirm that soot growth predominantly takes place in the stagnant region close to the nominal stagnation point ($X/L_I = 0$) where the number densities peak. The rate of increase in the residence time subsequently reduces sharply towards the HCP due to the imposed velocity gradient. Lin et al. [12] showed that for related laminar propene flames benzene concentrations increase rapidly over 10 ms. The subsequent soot inception via the formation of PAHs will add further to the latter value. The current cold flow velocities are in the range 36 to 54 times higher with the turbulence fluctuations 6 to 8.8 time higher than the applied cold flow velocities [12]. The resulting integral timescales of turbulence, see Table 1,
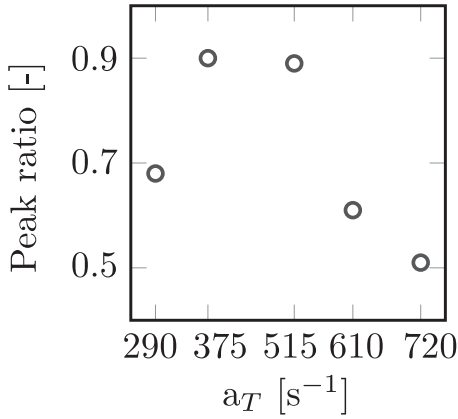
Fig. 8. Peak total number densities at various experimental conditions normalised relative to the reference flame ($\phi_{UN} = 2.0$, $a_T = 420$ s^{-1} and $T_{HCP} = 1500$ K). The total number densities are calculated based on the arithmetic average of the interval of $8 < D_m$ [nm] < 40.

are similar to the benzene formation rate and, accordingly, turbulent fluctuations will contribute to the distribution of soot inception related chemical species [2] throughout the turbulent flame brush. A direct consequence is that turbulence-chemistry interactions will strongly influence the rate of soot production.

The current number peak densities are in the range of $10^{12} < N$ [m^{-3}] $< 10^{16}$. The peak ratios of the total measured number densities as a function of the rate of strain are presented in Fig. 8 with the values normalised by the value for reference flame ($a_T = 420$ s^{-1}). The peak ratio of total number density increases by a factor of 1.47 when the total rate of strain is increased from $a_T = 290$ to 420 s^{-1}. By contrast, an increase in the rate of strain from $a_T = 420$ to 720 s^{-1} results in a reduction in the peak ratio by a factor of 0.51, suggesting a complex coupling between soot growth and oxidation.

The median and mean mobility diameters measured over the reaction zones are provided in Fig. 9 plotted against both physical distance and the estimated residence time. Peak values are found at the stagnation point irrespective of flame conditions and values remain below 10 nm for all flames. The current results can be compared to those obtained by Lin et al. [12] for a related laminar propene–air flames with cold gas velocities (U) in the range 3.75 to 5.0 cm·s^{-1} for flames with $\phi = 2.07$ (N1 to N4). The latter flames featured nozzle to stagnation plane separations (H) from 0.67 to 1.0 cm. The corresponding bulk rates of strain ($a_b = 2U/H$) for the laminar flame case with the highest [12] cold flow velocity (N4) can be estimated to be in the range $10 \leq a_b$ [s^{-1}] ≤ 15. The range of bulk rates of strain for the current flames
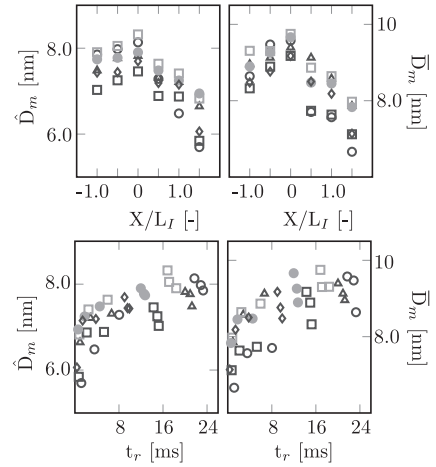

Fig. 9. Median (left) and mean (right) mobility size diameters for various flame conditions plotted against physical distance (top) and the estimated residence time (bottom). Open circle – $a_T = 290$ s^{-1} with $1.2 \leq t_r$ [ms] ≤ 23.3; triangle – $a_T = 375$ s^{-1} with $0.9 \leq t_r$ [ms] ≤ 21.3; grey square – $a_T = 420$ s^{-1} with $0.8 \leq t_r$ [ms] ≤ 18.4; black square – $a_T = 515$ s^{-1} with $0.7 \leq t_r$ [ms] ≤ 15.2; grey circle – $a_T = 610$ s^{-1} with $0.6 \leq t_r$ [ms] ≤ 12.7; diamond – $a_T = 720$ s^{-1} with $0.4 \leq t_r$ [ms] ≤ 9.9. X/L$_I > 0$ is towards reactants and X/L$_I < 0$ towards the hot combustion products.
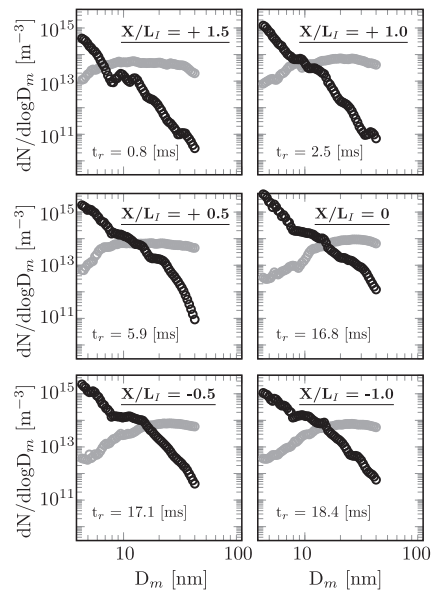

Fig. 10. Comparison of PSDs obtained using nano–DMA for ethene–air (grey circles) [7] and propene–air (black circles) with both flames at $a_T = 420$ s^{-1}, $\phi_{UN} = 2.0$ and $T_{HCP} = 1500$ K.

is $90 \leq a_b$ [s^{-1}] ≤ 180 due to the higher cold flow velocities with the total rate of strain estimated to $290 \leq a_T$ [s^{-1}] ≤ 720 due to the dominant turbulent contribution as shown in Table 1. The current rates of strain are accordingly 20 to 50 times higher and the impact is clear from the predominantly unimodal PSDs with the residence time too short for a bimodal shape to develop. The shorter residence times also lead to much reduced mobility size diameters that remain well below 10 nm, see Fig. 9, compared to values in the range of 30 to 70 nm for flames N1 to N4 [12]. However, the same sharp qualitative and quantitative differences between PSDs obtained in ethene–air and propene–air flames noted by Lin et al. [12] are present as exemplified in Fig. 10. The differences between the two fuels include an increase of around two orders of magnitude in the amount of smaller particles, indicating much faster soot inception in propene flames. The latter is consistent with the importance of the propargyl radical in benzene formation. However, it is also clear that the PSDs in the ethene–air flames shift towards larger particles more rapidly, suggesting that the parent fuel has a strong impact on the balance between soot inception and soot mass growth. Synergistic effects between ethene and propene have been observed in fuel mixtures with a small amount of ethene addition to propene causing more rapid growth of soot [13]. Overall, it is clear that PSDs are exceptionally sensitive to both the chemistry of the parent fuel and the flow field with the implication that accurate modelling of turbulence-chemistry interactions is essential for sooting turbulent flames.

5. Conclusions

An opposed jet configuration has been used to study the impact of the rate of strain on particle size distribution through the turbulent flame brush for propene–air flames. A series of six sooting flame was used to determine the dependence of PSDs on the rate of strain using SMPS equipped with nano– and long–DMA columns. Spatially resolved data along the stagnation point streamline show the evolution of PSDs through the turbulent flame brush and that turbulent transport distributes soot particles across the mixing layer between the two jets. Comparisons with results obtained in ethene–air flames [7] show that the particle size distributions are exceptionally sensitive to both the chemistry of the parent fuel and flow field conditions. However, while the total rates of strain exceed those of a corresponding study of laminar flames [12] by factors of 20 to 50, the qualitative trends observed in laminar flames remain. It has also been shown that the reduced residence times in turbulent flames strongly impact the growth of larger particles with the maximum median and mean mobility diameters remaining below 10 nm and that turbulent flow

conditions strongly favour unimodal PSDs. Nevertheless, bimodality can be expected to develop in regions of low rates of strain and the determination of the PDF of residence time at varying turbulence intensities is highly desirable. The latter can be investigated by keeping the bulk flow velocity constant while varying the turbulence intensity[1] This can be achieved by changing the specification of the fractal grid and guidance data is available [18]. Modest changes in the turbulent rate of strain can be expected to have significant impact on PSDs. The current detailed information on the dependence of PSDs on the parent fuel and flow conditions provides validation targets suitable for evaluation of the applicability of models for soot formation in turbulent flames.

Declaration of Competing Interest

The authors declare that they have no known competing financial interests or personal relationships that could have appeared to influence the work reported in this paper.

Supplementary material

Supplementary material associated with this article can be found, in the online version, at doi:10.1016/j.proci.2022.07.201.

References

[1] G. Blanquart, H. Pitsch, Analyzing the effects of temperature on soot formation with a joint volume-surface-hydrogen model, Combust. Flame 156 (2009) 1614–1626.

[2] H. Shariatmadar, F. Hampp, R.P. Lindstedt, The evolution of species concentrations in turbulent premixed flames crossing the soot inception limit, Combust. Flame 235 (2022) 111726.

---

[1] The authors would like to acknowledge that the suggestion was made by a referee as part of the peer review process.

[3] H. Shariatmadar, F. Hampp, R.P. Lindstedt, Quantification of PAH concentrations in premixed turbulent flames crossing the soot inception limit, Proc. Combust. Inst. 38 (2021) 1163–1172.

[4] W.R. Boyette, S. Chowdhury, W.L. Roberts, Soot particle size distribution functions in a turbulent non-premixed ethylene-nitrogen flame, Flow Turbul. Combust. 98 (2017) 1173–1186.

[5] P.M. de Oliveira, D. Fredrich, G. De Falco, I.E. Helou, A. D'Anna, A. Giusti, E. Mastorakos, Soot-free low-NOx aeronautical combustor concept: the lean azimuthal flame for kerosene sprays, Energy Fuel 35 (2021) 7092–7106.

[6] M. Kazemimanesh, R. Dastanpour, A. Baldelli, A. Moallemi, K.A. Thomson, M.A. Jefferson, M.R. Johnson, S.N. Rogak, J.S. Olfert, Size, effective density, morphology, and nano-structure of soot particles generated from buoyant turbulent diffusion flames, J. Aerosol Sci. 132 (2019) 22–31.

[7] H. Shariatmadar, P.G. Aleiferis, R.P. Lindstedt, Particle size distributions in turbulent premixed ethylene flames crossing the soot inception limit, Combust. Flame (2022) 11197.

[8] S. Gkantonas, M. Sirignano, A. Giusti, A. D'Anna, E. Mastorakos, Comprehensive soot particle size distribution modelling of a model Rich-Quench-Lean burner, Fuel 270 (2020) 117483.

[9] L. Tian, M.A. Schiener, R.P. Lindstedt, Fully coupled sectional modelling of soot particle dynamics in a turbulent diffusion flame, Proc. Combust. Inst. 38 (2021) 1365–1373.

[10] M.A. Schiener, R.P. Lindstedt, Transported probability density function based modelling of soot particle size distributions in non-premixed turbulent jet flames, Proc. Combust. Inst. 37 (2019) 1049–1056.

[11] M. Lucchesi, A. Abdelgadir, A. Attili, F. Bisetti, Simulation and analysis of the soot particle size distribution in a turbulent nonpremixed flame, Combust. Flame 178 (2017) 35–45.

[12] H. Lin, C. Gua, J. Camacho, B. Lin, C. Shao, R. Lia, H. Gu, B. Guan, H. Wang, Z. Huang, Mobility size distributions of soot in premixed propene flames, Combust. Flame 172 (2016) 365–373.

[13] B. Lin, H. Gu, H. Ni, B. Guan, Z. Li, D. Han, C. Gu, C. Shao, Z. Huang, H. Lin, Effect of mixing methane, ethane, propane and ethylene on the soot particle size distribution in a premixed propene flame, Combust. Flame 193 (2018) 54–60.

[14] B. Lin, H. Gu, B. Guan, D. Han, C. Gu, Z. Huang, H. Lin, Size evolution of soot particles from gasoline and n-heptane/toluene blend in a burner stabilized stagnation flame, Fuel 203 (2017) 135–144.

[15] C. Shao, F. Campuzano, Y. Zhai, H. Wang, W. Zhang, S.M. Sarathy, Effects of ammonia addition on soot formation in ethylene laminar premixed flames, Combust. Flame 235 (2022) 111698.

[16] A. Violi, A.D. Anna, A.D. Alessio, A.F. Sarofim, Modeling aerosol formation in opposed-flow diffusion flames, Chemosphere 10 (2003) 1047–1054.

[17] F. Hampp, S. Shariatmadar, R.P. Lindstedt, Quantification of low Damköhler number turbulent premixed flames, Proc. Combust. Inst. 37 (2019) 1047–1054.

[18] P. Geipel, K.H.H. Goh, R.P. Lindstedt, Fractal-generated turbulence in opposed jet flows, Flow, Turbul. Combust. 85 (2010) 397–419.

[19] K.H.H. Goh, P. Geipel, F. Hampp, R.P. Lindstedt, Flames in fractal grid generated turbulence, Fluid Dyn. Res. 45 (6) (2013) 061403.

[20] W.K. George, H.J. Hussein, Locally axisymmetric turbulence, J. Fluid Mech. 233 (1991) 1–23.

[21] F. Hampp, R.P. Lindstedt, Quantification of combustion regime transitions in premixed turbulent DME flames, Combust. Flame 182 (2017) 248–268.

[22] F. Hampp, R.P. Lindstedt, Strain distribution on material surfaces during combustion regime transitions, Proc. Combust. Inst. 36 (2017) 1911–1918.

[23] L.W. Kostiuk, K.N.C. Bray, T.C. Chew, Premixed turbulent combustion in counterflowing streams, Combust. Sci. Technol. 64 (1989) 233–241.

[24] R.P. Lindstedt, B.B.O. Waldheim, Modeling of soot particle size distributions in premixed stagnation flow flames, Proc. Combust. Inst. 34 (2013) 1861–1868.

[25] J. Camacho, C. Liu, C. Gu, H. Lin, Z. Huang, Q. Tang, X. You, C. Saggese, Y. Li, H. Jung, L. Deng, I. Wlokas, H. Wang, Mobility size and mass of nascent soot particles in a benchmark premixed ethylene flame, Combust. Flame 162 (2015) 3810–3822.

[26] TSI scanning mobility particle sizer spectrometer 3938, https://tsi.com/products/particle-sizers/particle-size-spectrometers/scanning-mobility-particle-sizer-spectrometer-3938/.